Perturbed Rankine vortices in surface quasi-geostrophic dynamics

B. J. HARVEY and M. H. P. AMBAUM

Department of Meteorology, University of Reading, UK

Abstract

An analytical dispersion relation is derived for linear perturbations to a Rankine vortex governed by surface quasi-geostrophic dynamics. Such a Rankine vortex is a circular region of uniform anomalous surface temperature evolving under quasi-geostrophic dynamics with uniform interior potential vorticity. The dispersion relation is analyzed in detail and compared to the more familiar dispersion relation for a perturbed Rankine vortex governed by the Euler equations. The results are successfully verified against numerical simulations of the full equations. The dispersion relation is relevant to problems including wave propagation on surface temperature fronts and the stability of vortices in quasi-geostrophic turbulence.

1 Introduction

The simplest model for a two-dimensional fluid is the familiar two-dimensional Euler equations and there are many studies of vortices in this system. This note is concerned with vortices in an alternative 2-dimensional geophysical fluid model which has received renewed interest recently, namely that of surface quasi-geostrophic (SQG) dynamics (see Held et al. (1995)). This system is relevant to quasi-geostrophic dynamics near horizontal boundaries, and it

has been applied to several different components of the atmosphere-ocean system including near-surface temperature anomalies in the atmosphere (Müller et al. (1989), Schär & Davies (1990), Ambaum & Athanasiadis (2007)), height perturbations of the tropopause (Juckes (1994), Juckes (1995), Tulloch & Smith (2006)) and upper-level density anomalies in the ocean (Lapeyre & Klein (2006)).

In the following we use the terminology of near-surface temperature anomalies in the atmosphere. Vortices which form in this system correspond to regions of anomalous surface temperature and are often called 'surface enhanced' vortices since the velocity field is strongest near the surface and decays with height. We consider vortices composed of circular patches of uniform anomalous temperature analogous to the Rankine vortex of the two-dimensional Euler system. We derive a dispersion relation for linear perturbations to such patches and present numerical tests of its validity.

The motivation is three-fold. Firstly, vortices commonly form in all of the physical situations to which SQG dynamics has been applied so an understanding of their behaviour is of strong interest. Secondly, the dynamics of waves at surface temperture fronts is of interest. The simplest case of an isolated 1-d temperature front is not a possible basic state under the SQG inversion operator since in this case the Green's function is not integrable. The circular case provides a de-singularized alternative. Finally, a comprehensive comparison between the 2-d Euler and SQG systems is of inherent interest as several components of the atmosphere–ocean system can arguably be modelled by either system or a system which lies between the two.

We express the SQG system as follows:

$$\frac{\mathrm{D}\theta}{\mathrm{D}t} = 0 \quad \text{at} \quad z = 0 \tag{1}$$

$$\text{and} \quad \nabla^2\psi = 0 \quad \text{in} \quad z > 0, \tag{2}$$

where θ is proportional to the potential temeprature anomaly and ψ is the streamfunction,

$\mathrm{D}/\mathrm{D}t = \partial/\partial t + u\partial/\partial x + v\partial/\partial y$ is the geostrophic Lagrangian derivative and (2) represents the condition of zero interior PV. The geostrophic variables are given by

$$(u, v, \theta) = (-\psi_y, \psi_x, \psi_z) \tag{3}$$

and u, v and θ are all assumed to decay at large z. Given a surface θ distribution, the inversion (2)-(3) then determines all other fields uniquely. In the following we surpress the z-dependence of all variables and consider only their surface values. The inversion of a surface temperature distribution $\theta(\mathbf{x})$, where $\mathbf{x} = (x, y)$, then has the Green's function $G(\mathbf{x}) = -(2\pi|\mathbf{x}|)^{-1}$ (Held et al. (1995)). In spectral space the inversion of the surface fields takes the form $\hat{\psi}(\mathbf{k}) = -\hat{\theta}(\mathbf{k})/|\mathbf{k}|$ where $\mathbf{k} = (k, l)$ is the horizontal wave vector, as can be shown by taking Fourier transforms of the full three-dimensional fields.

For the atmospheric lower boundary application, θ is the potential temperature anomaly scaled by $g/\theta_{00}N$, and therefore has the dimension of a velocity field, and z is the vertical coordinate scaled with the Prandtl ratio, N/f. Here the 'lower boundary' is usually interpreted as the top of the planetary boundary layer, θ_{00} is a constant background reference temperature, N is the buoyancy frequency and f the Coriolis parameter.

We write the surface temperature for the basic state Rankine vortex as

$$\theta = \Theta(r) \equiv \begin{cases} \theta_0 & r < a \\ \\ 0 & r > a \end{cases} \tag{4}$$

where r is the radial coordinate. That such a patch is stable, and therefore supports neutral perturbations, follows from the SQG analogue of Rayleigh's stability theorem applied in radial coordinates: exponential growth of linear perturbations is only possible if $\Theta'(r)$ takes positive and negative values. This was shown by Carton (2009) for the case of smooth temperature profiles. As with the Rayleigh theorem the extension to discontinuous profiles takes an intuitive form whereby temperature discontinuities are considered as regions of infinite gradient with the appropriate sign.

In section 2 we invert the basic state (4) analytically and derive a dispersion relation for linear perturbations to the patch boundary. In section 3 we present numerical tests of the dispersion relation before presenting a closing discussion and conclusions in section 4.

2 Dispersion relation

In the following we apply the SQG inversion in cylindrical coordinates. This is done by expanding the temperature field in terms of Bessel functions of the first kind, that is, by using Hankel transforms. The Bessel functions of the first kind, denoted J_n, form separable solutions to the three-dimensional Laplace equation with cylindrical symmetry since they satisfy

$$\nabla^2(\mathrm{J}_n(kr)\mathrm{e}^{\mathrm{i}n\varphi - kz}) = 0, \tag{5}$$

where (r, φ, z) are the usual cylindrical coordinates, k is a positive real number and n is an integer label of the modes. Therefore, if the surface temperature field is written as

$$\theta(r, \varphi) = \sum_{n=0}^{\infty} \int_0^{\infty} \hat{\theta}(k, n)\mathrm{J}_n(kr)\mathrm{e}^{\mathrm{i}n\varphi} k \, dk, \tag{6}$$

then the full three-dimensional temperature field is recovered by multiplying the integrand by e^{-kz}. From the fact that $\theta = \psi_z$, the corresponding surface streamfunction has the form

$$\psi(r, \varphi) = \sum_{n=0}^{\infty} \int_0^{\infty} \left(\frac{-\hat{\theta}(k, n)}{k} \right) \mathrm{J}_n(kr)\mathrm{e}^{\mathrm{i}n\varphi} k \, dk. \tag{7}$$

Comparing (6) and (7) we see that the inversion therefore has the familiar form of the spectral space SQG inversion, $\hat{\psi} = -\hat{\theta}/k$. The inverse of the transform (6) is given by

$$\hat{\theta}(k, n) = \frac{1}{2\pi} \int_0^{\infty} \int_0^{2\pi} \theta(s, \varphi')\mathrm{J}_n(ks)\mathrm{e}^{-\mathrm{i}n\varphi'} s \, d\varphi' \, ds, \tag{8}$$

as can be checked using the Bessel function orthogonality relation $\int_0^{\infty} \mathrm{J}_n(ks)\mathrm{J}_n(kr) k \, dk = \delta(r - s)/r$.

We now use this method to invert the basic state profile (4). Due to the azimuthal symmetry only the $n = 0$ term contributes in the expansion (6) so we write

$$\Theta(r) = \int_0^\infty \hat{\Theta}(k) \mathrm{J}_0(kr) k \, dk, \tag{9}$$

where the inverse is given by (8),

$$\hat{\Theta}(k) = \int_0^\infty \Theta(s) \mathrm{J}_0(ks) s \, ds. \tag{10}$$

Substituting for Θ from (4) and using the relation $\kappa \mathrm{J}_0(\kappa) = (\kappa \mathrm{J}_1(\kappa))'$, this inverse evaluates as

$$\hat{\Theta}(k) = \frac{\theta_0 a}{k} \mathrm{J}_1(ka). \tag{11}$$

The streamfunction induced by the basic state (4) is therefore given by

$$\Psi(r) = -\theta_0 a \int_0^\infty \frac{\mathrm{J}_1(ka)}{k^2} \mathrm{J}_0(kr) k \, dk, \tag{12}$$

and the corresponding basic state azimuthal velocity field, $U(r) = \partial \Psi / \partial r$, is

$$U(r) = \theta_0 \int_0^\infty \mathrm{J}_1(\kappa) \mathrm{J}_1(\kappa r/a) \, d\kappa, \tag{13}$$

where we have substituted $\kappa = ka$ and used a further relation, $\mathrm{J}_0'(\kappa) = -\mathrm{J}_1(\kappa)$. We now introduce the notation

$$\mathrm{E}_n(r/a) \equiv \int_0^\infty \mathrm{J}_n(\kappa) \mathrm{J}_n(\kappa r/a) \, d\kappa, \tag{14}$$

so that the function E_1 is proportional to the basic state azimuthal velocity field,

$$U(r) = \theta_0 \mathrm{E}_1(r/a). \tag{15}$$

The higher order E_n are used below to describe perturbation quantities. Figure 1A shows plots of the functions E_n for various n.

We derive some asymptotic results for the function E_1 in Appendix A. We show that the singularity in U at $r = a$ takes the form

$$U(r) \sim \frac{\theta_0}{\pi} (-\log |1 - (r/a)^2| + 4 \log 2 - 2) \tag{16}$$

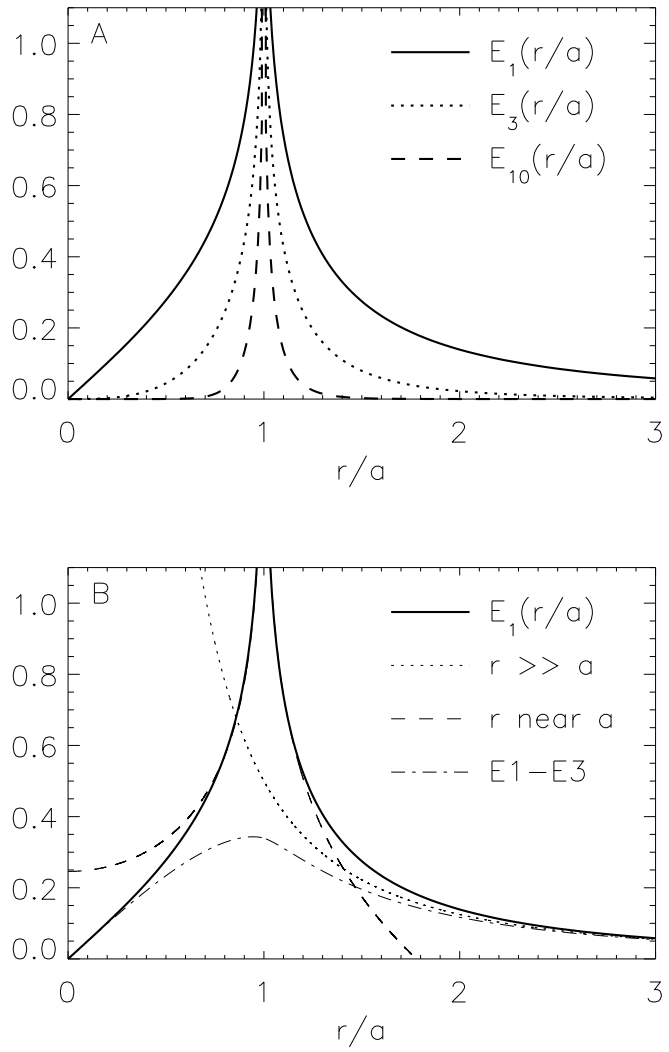

Figure 1: Panel A: Examples of the functions E_n. The solid line, E_1, is proportional to the basic state velocity profile, see (13). The cases $n > 1$ are proportional to the perturbation streamfunction of a mode n disturbance, see (24). Panel B: The dashed line is the asymptotic result for $|r/a - 1| \ll 1$ of (16) and the dotted line is the asymptotic result for $r \gg a$ of (17). Finally, the dot-dash line shows $\mathrm{E}_1 - \mathrm{E}_3$, see (26) and Appendix B, to illustrate that this combination if finite in the limit $r \to a$.

and this is consistent with other studies which show that θ discontinuities induce velocity fields with logarithmic singularities under SQG inversion (e.g. Held et al. (1995), Juckes (1995)). Note that since this singular velocity is directed parallel to the temperature discontinuity it does not induce a singular displacement of the discontinuity. Any perpendicular velocities turn out to be finite — see below. We also show in Appendix A that for $r \gg a$,

$$U(r) \sim \frac{\theta_0 a^2}{2r^2} \tag{17}$$

which is consistent with the form of the SQG Green's function, $G(\mathbf{x}) = -(2\pi|\mathbf{x}|)^{-1}$. Both of these asymptotic fits are plotted in figure 1B.

Next, we analyse the evolution of perturbations on the patch. Suppose the patch boundary is moved to the new position

$$r = R(\varphi, t) \equiv a + \eta(\varphi, t), \tag{18}$$

with $\eta \ll a$. We obtain the dispersion relation by considering the condition of material advection of this boundary, which is expressed formally as

$$\frac{DR}{Dt} \equiv \frac{\partial R}{\partial t} + \frac{u_\varphi}{R}\frac{\partial R}{\partial \varphi} = u_r \tag{19}$$

where u_r and u_φ are the radial and azimuthal components of the velocity field evaluated at $r = R$. Both u_r and u_φ are singular at the boundary but the combination in (19) represents the velocity component perpendicular to the boundary, which Held et al. (1995) show to be regular in general for temperature discontinuities. This can be checked directly for this case by expressing u_r and u_φ as contour integrals around the patch boundary (not shown). Juckes (1995) further demonstrates that the linear version takes the form

$$\frac{\partial \eta}{\partial t} = \lim_{r \to a}\left(u_r'(r, \varphi) - \frac{U(r)}{a}\frac{\partial \eta}{\partial \varphi}\right), \tag{20}$$

where $U(r)$ is the basic state velocity of (15) and u_r' is a linear version of the radial velocity field given by approximating the perturbation temperature distribution as a ring of δ-functions.

That is, by inverting

$$\theta(r,\varphi,t) = \Theta(r) + \theta_0\eta(\varphi,t)\delta(r-a). \tag{21}$$

This linearisation can also be verified directly for this case via the contour integral representation (not shown).

We invert the perturbation part of (21) using the transform (6). For each azimuthal mode, that is $\eta = \hat{\eta}(t)\mathrm{e}^{\mathrm{i}n\varphi}$, the transform of the final term in (21) takes the form

$$\eta(\varphi,t)\delta(r-a) = \hat{\eta}(t)\mathrm{e}^{\mathrm{i}n\varphi}\int_0^\infty \hat{\delta}(k)\mathrm{J}_n(kr)k\,dk \tag{22}$$

where $\hat{\delta}(k)$ is given by (8)

$$\hat{\delta}(k) = \int_0^\infty \delta(s-a)\mathrm{J}_n(ks)s\,ds = a\mathrm{J}_n(ka). \tag{23}$$

The induced perturbation streamfunction is therefore

$$\psi(r,\varphi,t) = -\theta_0\hat{\eta}(t)e^{\mathrm{i}n\varphi}\int_0^\infty \mathrm{J}_n(\kappa)\mathrm{J}_n(\kappa r/a)\,d\kappa = -\theta_0\hat{\eta}(t)e^{\mathrm{i}n\varphi}\mathrm{E}_n(r/a), \tag{24}$$

using the notation introduced in (14), and the corresponding perturbation radial velocity field, $u_r' = -r^{-1}\partial\psi/\partial\varphi$, is given by

$$u_r'(r,\varphi) = \frac{\mathrm{i}n}{r}\theta_0\hat{\eta}(t)\mathrm{E}_n(r/a)\mathrm{e}^{\mathrm{i}n\varphi}. \tag{25}$$

Finally, we substitute for U and u_r' in (20) and put $\hat{\eta}(t) \propto \mathrm{e}^{-\mathrm{i}\omega_n t}$ to give

$$\omega_n = \frac{\theta_0 n}{a}\lim_{r\to a}(\mathrm{E}_1(r/a) - \mathrm{E}_n(r/a)). \tag{26}$$

This limit is finite, as illustrated in figure 1B for the case $n = 3$. In Appendix B we evaluate the limit analytically for all n via a recursion relation and find that the dispersion relation can be written as

$$\boxed{\omega_n = \frac{\theta_0 n}{a}\frac{2}{\pi}\sum_{j=2}^{n}\left(\frac{1}{2j-1}\right)} \tag{27}$$

for $n \geq 2$. The case $n = 1$ has, trivially, $\omega_1 = 0$. The limit in (26) can also be evaluated for non-integer values of n, the result being continuous, but this case is not so analytically

tractable or physically relevant. The dispersion relation (27) is the main result of this paper. Below we examine its properties in detail and in section 3 we verify it numerically.

First, we note for comparison the corresponding result for linear perturbations to a barotropic Rankine vortex, that is, a patch of uniform vorticity evolving under the two-dimensional Euler equations. Taking Ω as the uniform patch vorticity the dispersion relation is (see Saffman (1995))

$$\omega_n = \frac{\Omega}{2}(n-1). \tag{28}$$

For both of these cases, (27) and (28), the corresponding phase and group speeds can be calculated as

$$c_{\mathrm{p},n} = \frac{a\omega_n}{n} \quad \text{and} \quad c_{\mathrm{g},n+1/2} = a(\omega_{n+1} - \omega_n) \tag{29}$$

respectively. Note that the SQG phase speeds are independent of the patch radius whereas the barotropic phase speeds are proportional to the patch radius, a result which is obvious from dimensional grounds. Figure 2 shows plots of the phase and group speeds as functions of wavenumber, n. We have non-dimensionalised the speeds by θ_0 in the SQG case and $a\Omega$ in the barotropic vorticity case.

To analyse the form of the SQG dispersion relation (27) we note that for large n (see Gradshteyn & Ryzhik (2000)):

$$\sum_{j=2}^{n} \left(\frac{1}{2j-1} \right) = \frac{1}{2}(\log n + \gamma) + \log 2 - 1 + \mathrm{O}(n^{-2}), \tag{30}$$

where $\gamma = 0.57721...$ is Euler's constant. The dispersion relation (27) therefore satisfies

$$\omega_n = \frac{\theta_0}{\pi a} n(\log n + \mu) + \mathrm{O}(n^{-1}), \tag{31}$$

where $\mu = \gamma + 2(\log 2 - 1) \approx -0.03649$. Truncating the $\mathrm{O}(n^{-2})$ terms gives a remarkably accurate approximation with fractional errors of only 1.5% for $n = 2$ and 0.4% for $n = 3$. The solid lines in figure 2A show this accuracy visually for the corresponding phase and group speeds, group speed now defined as $c_g = a\partial\omega_n/\partial n$, and table (1) shows the values numerically.

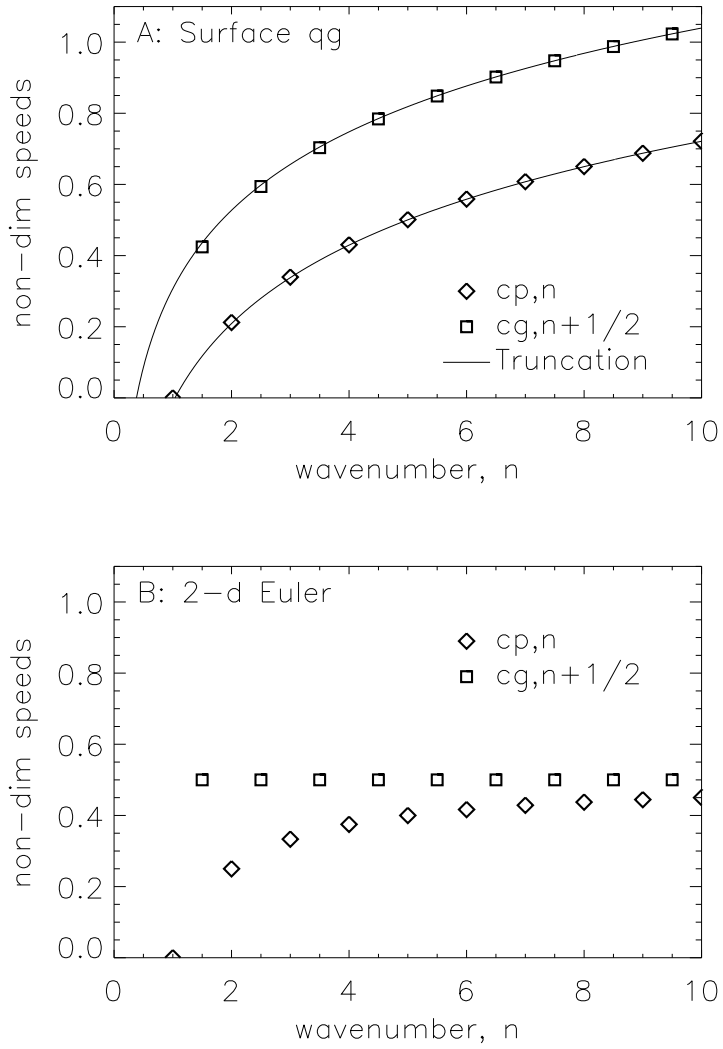

Figure 2: Non-dimensional phase and group speeds (c_p and c_g respectively) for the SQG (panel A) and two-dimensional Euler (panel B) systems. Symbols mark the exact analytic results of (27) and (28). The lines in panel A show the corresponding quantities for the truncated version of the dispersion relation (31).

This truncated version of the dispersion relation has the same form as that of waves on straight θ discontinuities which is (taken implicitly from Juckes (1995))

$$\omega = \frac{\Delta\theta}{\pi} k(\log k + C) \tag{32}$$

where k is the perturbation wavenumber, $\Delta\theta$ the size of the θ discontinuity and C a constant depending on the basic state velocity profile. It is worthy of note that the natural choice of basic state for studying waves at θ discontinuities, a single 1-d temperature Heaviside discontinuity, is not invertible under the SQG inversion operator. Any other 1-d profile must contain at least one additional lengthscale and this will balance the dimension of k in the logarithm. Any other profile will also, however, contain additional regions of non zero temperature gradient which will influence the wave propagation at the discontinuity so (32) is only a local approximation.

Finally we note that the dispersion relation for the SQG Rankine vortex (27) satisfies a peculiar group speed–phase speed relation,

$$c_{\mathrm{g},n+1/2} = \frac{1}{2}(c_{\mathrm{p},n} + c_{\mathrm{p},n+1}) + \frac{\theta_0}{\pi}. \tag{33}$$

This relation also holds for waves on a straight θ discontinuity (32) in that

$$\frac{\partial\omega}{\partial k} = \frac{\omega}{k} + \frac{\Delta\theta}{\pi}. \tag{34}$$

This result is independent of any ambiguities associated with the basic state velocity profile and appears to be a robust property of perturbations at θ discontinuities.

3 Numerical verification

Here we verify the dispersion relation of (27) via numerical simulation of temperature patches in an SQG model.

The numerical model runs on a $[0,1]\times[0,1]$ doubly periodic domain. The time integration is performed with a semi-Lagrangian advection scheme consisting of a second order back-trajectory calculation and bicubic spatial interpolation. The temporal resolution is varied dynamically via a Lifschitz criterion such that $|\nabla \mathbf{u}|\Delta t < C$ where we choose $C = 0.3$ for the tests presented here. The temperature field inversion is performed using Fourier transforms and the spatial resolution used here is 512 gridpoints in each direction. We have repeated the calculations at various resolutions and found we could verify the dispersion relation at these resolutions as well.

We specify the initial condition in the model as a circular patch of anomalous θ with a small amplitude, single wavenumber perturbation of its circumference and then sum, at each time step, the squared differences between the current and the initial states,

$$\sum_{\text{gridpoints}} \left(\theta(t) - \theta(0)\right)^2 . \tag{35}$$

We find the location of the first minimum in this time series using a quadratic fitting technique and this corresponds to the time taken for the perturbation to rotate through an angle of $2\pi/n$, which we write as $\tilde{t}_n$ (we use the tilde to denote numerically obtained values). The corresponding nondimensionalised phase speed is then given by $\tilde{c}_{\mathrm{p},n} = 2\pi a/n\tilde{t}_n\theta_0$.

Table 1 shows that the best estimate of the phase speeds achieved from the numerics is within a suitably defined error of the analytic result for a range of wavenumbers and this therefore verifies the result. However, our model in not ideally designed for this simulation[1] and several issues had to be carefully considered. We discuss these now.

Firstly, the sharp gradients in the basic state (4) cannot be accurately represented by any grid-based numerical scheme. We choose instead to simulate a smooth version of the profile

[1] A pure contour dynamics method (e.g. Zabusky et al. (1979), Pullen (1992)) appears to be the most natural choice, but this suffers from the logarithmic singularity in the along-front velocity field.

given by

$$\Theta(r) = \frac{1}{2}\left\{1 - \tanh\left[\frac{r - a(1 + \epsilon\cos(n\varphi))}{\delta}\right]\right\}, \tag{36}$$

where δ and ϵ are measures of the edge steepness and perturbation amplitude respectively. This profile is well behaved numerically for a wide range of δ and by systematically varying δ and then extrapolating to $\delta = 0$ we can verify that the numerical results are consistent with the analytic result of section 2. It is shown implicity in Juckes (1995) that the leading order effect of a slight smoothing of width δ to a θ discontinuity is a reduction in the perturbation phase speeds of the form

$$c_p^{\text{smooth}} \sim c_p - B\delta^2 \log(\delta/\delta_0) \tag{37}$$

where B and δ_0 are constants depending on the form of the smoothing and the wavenumber of the perturbation. We use this form of the correction to extrapolate our numerical results to the limit of $\delta \to 0$. We plot in figure 3A some numerically obtained phase speeds for the profile (36) for various values of δ and $n = 3$. Also plotted is the fit (37) where c_p, B and δ_0 are the fitting parameters. The variation of numerical phase speed with smoothing width is captured well by this fit.

We estimate an error in the extrapolated phase speed value based on resolution effects as follows. We first calculate the number of gridpoints covered by the smoothed patch-edge region along a cross section of the patch in each experiment. We then calculate the error estimate by comparing the variation of this number accross the range of experiments performed with the variation of the corresponding phase speeds obtained and assume that the finite numerical resolution introduces an error in the effective smoothing width of $\pm 1/2$ gridsize. We refer to this error estimate further below.

The other issue with the numerical scheme is the domain periodicity. This domain is equivalent to performing the inversion on an unbounded domain with an infinite array of identical patches centred at coordinates (i, j), with i and j integers. These patches have basic

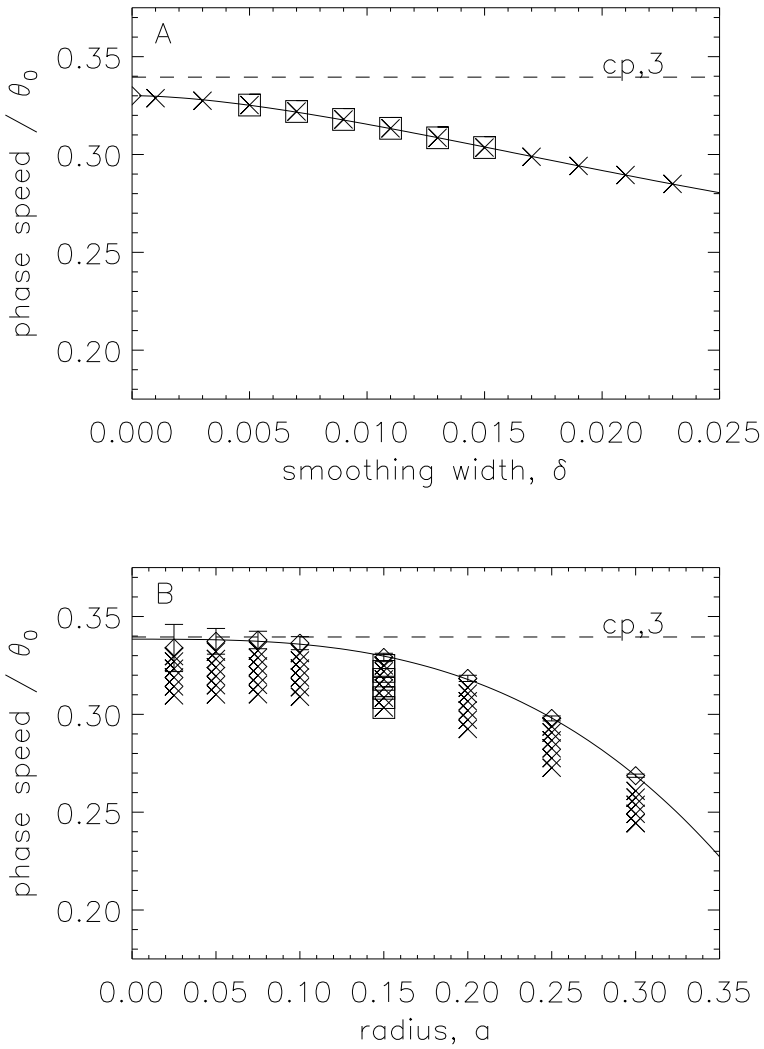

Figure 3: Panel A: Numerically obtained phase speeds versus δ for the case $a = 0.15$, $\epsilon = 0.00667$ and $n = 3$; solid line is nonlinear fit of (37), dashed line is analytic result $c_{\mathrm{p},3}$ and squares show the values used for panel B. Panel B: Numerically obtained phase speeds versus a for the case $\epsilon = 0.00667$ and $n = 3$; diamonds are extrapolations to $\delta \to 0$ with associated error bar (see text), solid line is nonlinear fit for periodicity (39) and dashed line is again $c_{\mathrm{p},3}$.

state circulations of the same sign as the central patch and therefore induce an opposite circulation around the central vortex. This induced circulation reduces the phase speed compared to the non-periodic case. The magnitude of this effect is a function of the patch radius so we have repeated the above extrapolation process for a range of a values and present the results in figure 3B, again for the case $n = 3$. Note that, since the fit (37) appears to be fairly robust, we use fewer δ values here than in figure 3A to save computation time.

The fitted line in figure 3B is based on the following estimation of the combined influence of the surrounding patches. The effect is not exactly isotropic around the circumference of the patch, but tests have shown the anisotropic component to be small for reasonable a values. Consider just three patches aligned linearly and spaced a distance L apart. The far-field effect of the outer two patches on the central patch cancels at leading order, meaning that the central patch does not move. Higher order terms act as a local adverse shearing. For example, at the point where the central patch meets the line joining the three patches the induced velocity parallel to the patch boundary is

$$U(L+a) - U(r-a) \approx -2\theta_0 \frac{a^3 L}{(L^2 - a^2)^2}. \tag{38}$$

The approximation here is from the expansion (17). This correction takes the value $0.017\theta_0$ for $a = 0.2, L = 1$ which accounts for much of the discrepancy in figure 3B for that case. We estimate the total effect of all the patches as the sum of (38) over many of the nearest neighbours multiplied by a constant to take account of the anisotropy. That is, we fit

$$c_{\mathrm{p}}^{\mathrm{periodic}} \sim c_{\mathrm{p}} - Ca^3 \sum_{i>0, j\geq 0} \left(\frac{L_{i,j}}{(L_{i,j}^2 - a^2)^2} \right) \quad \text{with} \quad L_{i,j} = \sqrt{i^2 + j^2} \tag{39}$$

to the data in figure 3B by varying c_{p} and C. In practice we avoid the slow convergence of the sum by truncating it to $i, j \leq 3$ and estimate the rest of the sum with an additional fitting constant, D. The data is weighted in the fit according to the resolution error decribed above at each radius value and the corresponding fitting error, σ_{fit}, of the best estimate phase speed

is calculated and presented in table 1. The best estimate phase speed, given by the fitted value of $c_{\rm p}$, is also shown. The analytic result of section 2 lies within $\sigma_{\rm fit}$ of the numerically obtained value.

In summary, by extrapolating to the double limit of $\delta,\ a \to 0$ we have shown that, to within a calculated resolution error, the analytic result of section 2 is correct for the case $n = 3$. We have repeated this process for a range of different wavenumbers and the results are also summarised in table 1. In each case the numerical result lies within $2\sigma_{\rm fit}$ of the analytic result. Noticably, all numerically obtained phase speeds are slower than the analytic value and this suggests that other systematic errors are present which have not been taken into acount. However, they appear to be not much larger than the resolution error. The most likely candidates are the accuracy of the back-trajectory calculation in the semi-Lagrangian scheme, the hyper-diffusion like effects associated with interpolation used in the semi-Lagrangian scheme and nonlinear amplitude effects on the wave propagation.

4 Conclusions

We have derived and tested a dispersion relation for perturbations to the edge of a circular patch of uniform temperature evolving under SQG dynamics. The dispersion relation is similar to that of waves on a straight 1-d temperature discontinuity. However, unlike the 1-d profile result, the patch solution is global.

The dispersion relation shows qualitative similarities to its two-dimensional Euler counterpart and it is expected that further results from barotropic vortices carry over to the SQG case. For instance, under two-dimensional Euler dynamics there are nonlinear perturbations to uniform vorticity patches which rotate steadily, the so-called V-states (Deem & Zabusky (1978), Verkley (1994), Ambaum & Verkley (1995)), and we expect there to be SQG analogues. In fact, each mode of the linear dynamics in the barotropic case is associated with

such a solution and we expect that the linear modes found here are likewise related to SQG V-state solutions.

A further inference from our result concerns the behaviour of SQG vortices embedded within a background flow. Such a flow will in general deform the vortex in a time dependent manner. For the simple case of a pure straining, $(u, v) = s(x, -y)$, there are illuminating steady state solutions in the small strain rate limit, $s \ll \theta_0/a$ (assuming s and θ_0 are both positive). In that case the deformation is small and so satisfies the dispersion relation (27). The $n = 2$ mode can propagate against the straining flow resulting in a steady state provided its phase speed matches the induced rotation speed of the straining which can be shown to be given by $c_{\rm rot} = -a^2 s/2\eta_0$, where η_0 is the perturbation amplitude. Equating this to $c_{\rm p,2}$ from (29) we find the steady state requires

$$\frac{\eta_0}{a} = \frac{3\pi}{4}\frac{as}{\theta_0}. \tag{40}$$

Interestingly, this perturbation aspect ratio is proportional to the patch radius so a small vortex will not deform as strongly as a large vortex in the same straining field. Alternatively, this result suggests that small vortices require stronger strain values to cause vortex break-up than a larger vortex and this is consistent with the local nature of the SQG Green's function. This has obvious consequences for the flow morphology of SQG turbulence. In contrast, the corresponding two-dimensional Euler result predicts a perturbation aspect ratio of $\eta_0/a = 2s/\Omega$ which is independent of vortex size. Whether (40) can be generalized to finite amplitudes as in the case of the Kida vortex is still an open question.

A

Asymptotics of $\mathrm{E}_1(r/a)$

Here we derive the two asymptotic results for the function E_1 which are referred to in section 2, equations (16) and (17).

A.1 Small $|r/a - 1|$

The calculation in Appendix B shows that the leading order term of the singularity at $r = a$ is the same for each of the E_n. Here we show that E_0 is actually a complete elliptic integral of the first kind for which there are well known asymptotic results and then the result for E_1 follows. To do this we use the following integral definition of the Bessel functions which is suitable when n is an integer:

$$\mathrm{J}_n(\kappa) = \frac{1}{2\pi}\int_{-\pi}^{\pi} \mathrm{e}^{\mathrm{i}(\kappa\sin\theta - n\theta)}\, d\theta. \tag{41}$$

Substituting for J_0 in (14) gives

$$\mathrm{E}_0(\rho) = \frac{1}{4\pi^2}\int_{-\pi}^{\pi}\int_{-\pi}^{\pi}\int_{0}^{\infty} \mathrm{e}^{\mathrm{i}\kappa(\sin\theta + \rho\sin\phi)}\, d\kappa\, d\theta\, d\phi \tag{42}$$

where we have put $\rho = r/a$. Upon use of the identity

$$\int_0^\infty \mathrm{e}^{\mathrm{i}\kappa f(x)}\, d\kappa = \pi \sum_{\{x_i : f(x_i)=0\}} \frac{\delta(x - x_i)}{|f'(x_i)|}, \tag{43}$$

the integral (42) can be written as

$$\mathrm{E}_0(\rho) = \frac{2}{\pi}\int_0^{\pi/2} \frac{d\phi}{(1 - \rho^2\sin^2\phi)^{1/2}}. \tag{44}$$

This is a standard definition of the complete elliptic integral of the first kind. It therefore follows from a standard result (Gradshteyn & Ryzhik (2000)) that

$$\mathrm{E}_0(\rho) \approx \frac{2}{\pi}\left(-\frac{1}{2}\log|1 - \rho^2| + 2\log 2\right) \tag{45}$$

near $\rho = 1$, and so, by rearranging (57) to find

$$\lim_{\rho\to 1}(\mathrm{E}_1(\rho) - \mathrm{E}_0(\rho)) = -\frac{2}{\pi}, \tag{46}$$

we arrive at

$$\mathrm{E}_1(\rho) \approx \frac{1}{\pi}(-\log|1-\rho^2| + 4\log 2 - 2). \tag{47}$$

A.2 Large r/a

The $n = 1$ version of (42) is

$$\mathrm{E}_1(\rho) = \frac{1}{4\pi^2}\int_{-\pi}^{\pi}\int_{-\pi}^{\pi}\int_0^{\infty} \mathrm{e}^{\mathrm{i}\kappa(\sin\theta+\rho\sin\phi)}\mathrm{e}^{-\mathrm{i}(\theta+\phi)}\,d\kappa\,d\theta\,d\phi. \tag{48}$$

With the aim of using (43) again, note that for large ρ the zeros of the first exponential occur at $\phi \approx -\rho^{-1}\sin\theta$ and $\phi \approx \pm\pi + \rho^{-1}\sin\theta$. On substituting into (48) and rearranging we arrive at

$$\mathrm{E}_1(\rho) \approx \frac{1}{2\pi}\int_{-\pi}^{\pi} \frac{\sin\theta \sin\left(\frac{\sin\theta}{\rho}\right)}{\rho|\cos\left(\frac{\sin\theta}{\rho}\right)|}\,d\theta \tag{49}$$

$$\approx \frac{1}{2\pi\rho^2}\int_{-\pi}^{\pi}\sin^2\theta\,d\theta \tag{50}$$

$$= \frac{1}{2\rho^2}. \tag{51}$$

Similarly it can be shown that $\mathrm{E}_n(\rho) \propto \rho^{-(n+1)}$ for large ρ.

B

Calculation of limit in (26)

Here we evaluate the limit in (26), which we denote as α_n:

$$\alpha_n = \lim_{\rho\to 1}\left(\mathrm{E}_1(\rho) - \mathrm{E}_n(\rho)\right) = \int_0^{\infty}\left(\mathrm{J}_1(\kappa)\mathrm{J}_1(\kappa) - \mathrm{J}_n(\kappa)\mathrm{J}_n(\kappa)\right)d\kappa. \tag{52}$$

These intregrals are finite even though the two individual components are not. Substituting for the integral representation (41) gives

$$\alpha_n = \frac{1}{4\pi^2}\int_{-\pi}^{\pi}\int_{-\pi}^{\pi}\int_0^{\infty} \mathrm{e}^{\mathrm{i}\kappa(\sin\theta+\sin\phi)}(\mathrm{e}^{-\mathrm{i}(\theta+\phi)} - \mathrm{e}^{-\mathrm{i}n(\theta+\phi)})\,d\kappa\,d\theta\,d\phi. \tag{53}$$

Upon using the identity (43), where here the exponent vanishes for $\theta = -\phi$ and $\theta = \phi \pm \pi$ for $\phi >< 0$, we find

$$\alpha_n = \frac{1}{4\pi}\left(\int_{-\pi}^{0} \frac{\mathrm{e}^{-\mathrm{i}(2\phi+\pi)} - \mathrm{e}^{-\mathrm{i}n(2\phi+\pi)}}{|\cos\phi|} d\phi + \int_{0}^{\pi} \frac{e^{-i(2\phi-\pi)} - e^{-in(2\phi-\pi)}}{|\cos\phi|}\, d\phi\right), \tag{54}$$

which can be written as

$$\alpha_n = \frac{1}{2\pi}\int_0^{\pi} \frac{\cos\theta - \cos n\theta}{\sin(\theta/2)}\, d\theta \tag{55}$$

by writing $\theta = 2\phi + \pi$ and $\theta = 2\phi - \pi$ in the first and second integrals respectively. This integral can now be solved iteratively by considering α_{n+1} and expanding the cosine via the trigonometric summation formulae. After further use of standard trigonometric identities we arrive at

$$\alpha_{n+1} = \alpha_n + \frac{1}{\pi}\int_0^{\pi} \sin\left[(n+\frac{1}{2})\theta\right]\, d\theta \tag{56}$$

$$= \alpha_n + \frac{2/\pi}{2n+1}. \tag{57}$$

So, noting from (52) that $\alpha_1 = 0$, the result we are after is

$$\alpha_n = \frac{2}{\pi}\sum_{j=2}^{n}\left(\frac{1}{2j-1}\right). \tag{58}$$

References

Ambaum, M. H. P. & Athanasiadis, P. J. 2007 The response of a uniform horizontal temperature gradient to heating. *J. Atmos. Sci.* **64**, pp. 3708–3716.

Ambaum, M. H. P. & Verkley, W. T. M. 1995 Orography in a contour dynamics model of large-scale atmospheric flow. *J. Atmos. Sci.* **52**, pp. 2643–2662.

Carton, X. 2009 Instability of Surface Quasigeostrophic Vortices. *J. Atmos. Sci.* **66**, pp. 1051–1062.

Deem, G. S. & Zabusky, N. J. 1978 Vortex waves: stationary "V-states", interactions, recurrance and breaking. *Phys. Rev. Lett.* **40**, pp. 859–862.

Gradshteyn, I. S. & Ryzhik, I. M. 2000 *Table of Integrals, Series and Products.* AP, 6th edition.

Held, I. M., Pierrehumbert, R. T., Garner, S. T. & Swanson, K. L. 1995 Surface quasi-geostrophic dynamics. *J. Fluid Mech.* **282**, pp. 1–20.

Juckes, M. 1994 Quasigeostrophic dynamics of the tropopause. *J. Atmos. Sci.* **51**, pp. 2756–2768.

Juckes, M. 1995 Instability of surface and upper-tropospheric shear lines. *J. Atmos. Sci.* **52**, pp. 3247–3262.

Lapeyre, G. & Klein, P. 2006 Dynamics of the upper oceanic layers in terms of surface quasigeostrophy theory. *J. Phys. Ocean.* **36**, pp. 165–176.

Müller, J. C., Davies, H. C. & Schär, C. 1989 An unsung mechanism for frontogenesis and cyclogenesis. *J. Atmos. Sci.* **46**, pp. 3664–3672.

Pullen, D. I. 1992 Contour dynamics methods. *Ann. Rev. Fluid Mech.* **24**, pp. 89–115.

Saffman, P. G. 1995 *Vortex Dynamics.* CUP.

Schär, C. & Davies, H. C. 1990 An Instability of Mature Cold Fronts. *J. Atmos. Sci.* **47**, pp. 929–950.

Tulloch, R. & Smith, K. S. 2006 A Theory for the atmospheric energy spectrum: Depth-limited temperature anomalies at the tropopause. *Proc. Natl. Acad. Sci. USA* **103**, pp. 690–694.

Verkley, W. T. M. 1994 Tropopause dynamics and planetary waves. *J. Atmos. Sci.* **51**, pp. 509–529.

Zabusky, N. J., Hughes, M. H. & Roberts, K. V. 1979 Contour dynamics of the Euler equations in two dimensions. *J. Comput. Phys.* **30**, pp. 96–106.

Table 1: Analytic and numerically obtained phase speed values, nondimensionalised with θ_0. Also shown are the corresponding fitting error, see text, and numerical values from the truncated formula (31).

Wavenumber	Analytical phase speed	Numerical result	Fitting error	Truncated formula
n	$c_{\mathrm{p},n}$	$\tilde{c}_{p,n}$	σ_{fit}	$n(\log n + \mu)/\pi$
2	0.2122	0.2091	0.0012	0.2090
3	0.3395	0.3384	0.0020	0.3380
4	0.4305	0.4274	0.0025	0.4297
5	0.5012	0.4953	0.0022	0.5007
6	0.5591	0.5522	0.0032	0.5587
7	0.6081	0.5996	0.0040	0.6078
8	0.6505	0.6401	0.0046	0.6503